Geophysical Research Letters

RESEARCH LETTER
10.1029/2020GL090323

Key Points:

- Australia suffered a long-lasting extensive drought in 2019, the worst record in the recent four decades
- This extreme drought can be well explained by combined effects of the westernmost-located CP El Niño and third strongest positive Indian Ocean Dipole (IOD) events
- Severe Australian droughts could occur more frequently in a warming world with projected increases in both CP El Niño and extreme IOD events

Supporting Information:

- Supporting Information S1

Correspondence to:
W. Zhang,
zhangwj@nuist.edu.cn

Citation:
Zhang, W., Mao, W., Jiang, F., Stuecker, M. F., Jin, F-F., & Qi, L. (2021). Tropical Indo-Pacific compounding thermal conditions drive the 2019 Australian extreme drought. *Geophysical Research Letters*, *48*, e2020GL090323. https://doi.org/10.1029/2020GL090323

Received 12 AUG 2020
Accepted 9 DEC 2020

Tropical Indo-Pacific Compounding Thermal Conditions Drive the 2019 Australian Extreme Drought

Wenjun Zhang[1], Wei Mao[1], Feng Jiang[1], Malte F. Stuecker[2], Fei-Fei Jin[3], and Li Qi[1]

[1]CIC-FEMD/ILCEC, Key Laboratory of Meteorological Disaster of Ministry of Education (KLME), Nanjing University of Information Science and Technology, Nanjing, China, [2]Department of Oceanography & International Pacific Research Center (IPRC), School of Ocean and Earth Science and Technology, University of Hawai'i at Mānoa, Honolulu, HI, USA, [3]Department of Atmospheric Sciences, School of Ocean and Earth Science and Technology, University of Hawai'i at Mānoa, Honolulu, HI, USA

Abstract Australia suffered a long-lasting extensive drought in 2019 with catastrophic wildfires creating about $4.4 billion damages, the worst record in the recent four decades. Concurrent with this extreme drought, the tropical Indo-Pacific oceans exhibited an extraordinary combination of sea surface temperature (SST) anomalies, characterized by a Central-Pacific (CP) El Niño event with westernmost location and the third strongest positive Indian Ocean Dipole (IOD) event. We here show evidence that this unique combination was responsible for the pan-Australian drought as a westward located CP El Niño event and a strong positive IOD event can exacerbate precipitation reduction in northeastern and southern Australia, respectively. These continent-wide extreme droughts could become more frequent over Australia in a warming world, considering projected increases in both CP El Niño and extreme positive IOD events superimposed on secular warming and drying trends.

Plain Language Summary Australia is the driest inhabited continent in the world, 70% of which is either arid or semiarid land. During 2019, Australia was ravaged by the worst drought in decades with devastating wildfires destroying around 3,000 homes and affecting about one billion animals. The physical mechanisms driving this extreme drought remains unclear. Concurrent with this long-lasting continent-wide drought, the Indo-Pacific oceans showed pronounced sea surface temperature anomalies associated with a record westernmost-located Central Pacific (CP) El Niño event and the third strongest Indian Ocean Dipole (IOD) event co-occurring. Our observational diagnostics and numerical model experiments show that these two compounding events caused atmospheric circulation anomalies that were responsible for the extreme precipitation deficiencies over Australia. With global warming, both CP El Niño and extreme positive IOD events are projected to become more frequent, which hints to increased risk of the severe Australian droughts in the future.

1. Introduction

As one of the world's driest inhabited continents with a highly variable climate, Australia is frequently subject to prolonged and intensive droughts on seasonal to interannual timescales (Gallant et al., 2007; King et al., 2020; Ummenhofer et al., 2009). The year 2019 was characterized by prominent precipitation deficiencies and an extensive drought with devastating wildfires over Australia (Bureau of Meteorology, 2019a, Bureau of Meteorology, 2019b; Ell, 2020; see also Figure 1). It was the driest year on record across Australia as a whole in the recent four decades, suffering the strongest fire weather danger with high values in areas of all States and Territories (Bureau of Meteorology, 2019b). Understanding the mechanisms that led to this disastrous drought is of importance not only for assessing potential predictability of extreme droughts, but also for improving future resource management and strategic wildfire prevention.

The 2019 extreme drought witnessed remarkable sea surface temperature (SST) anomalies in the tropical Pacific and Indian oceans (Figure 2a). SST warming was evident in the Central Pacific throughout almost all seasons of 2019, which was classified as a moderate El Niño event by the Climate Prediction Center (CPC). El Niño, the warm phase of the El Niño-Southern Oscillation (ENSO), features a large-scale SST warming in the central and eastern equatorial Pacific in concert with coupled changes of the atmospheric circulation (McPhaden et al., 2006; Philander, 1990). Impacts of ENSO on Australian precipitation have

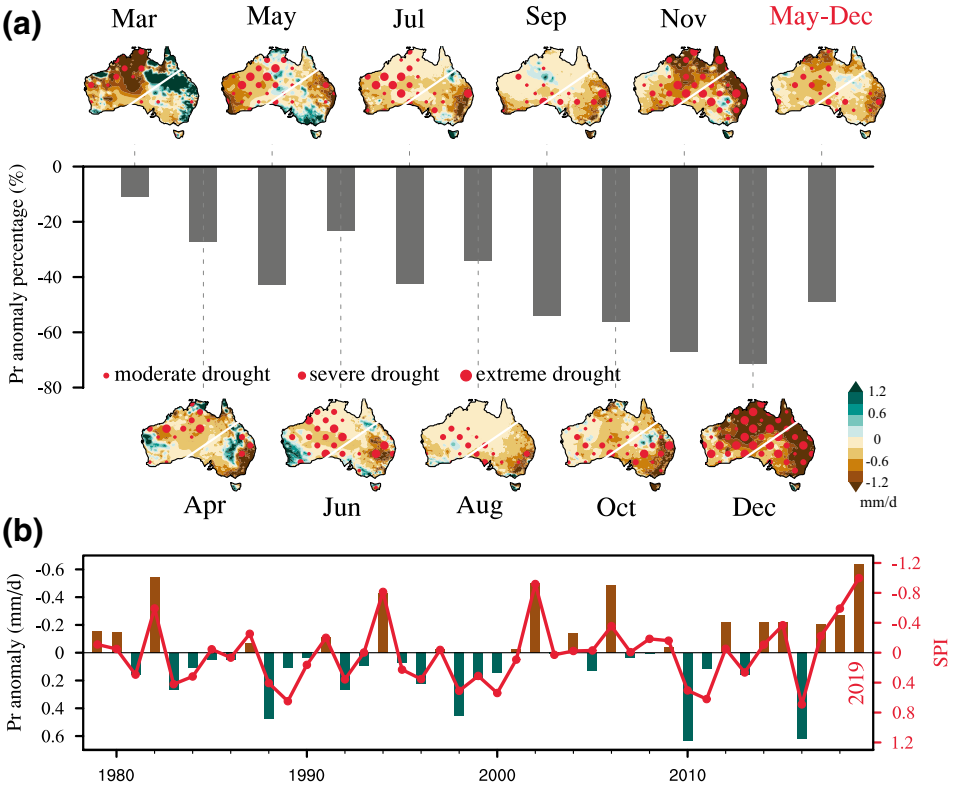

Figure 1. (a) Precipitation anomalies (shading; mm/d) superimposed by 6-month Standardized Precipitation Index (SPI; red dots) and all-Australian precipitation anomaly percentage relative to the climatological (1979–2019) condition (bar; %) from March to December 2019. (b) May to December averaged all-Australian precipitation anomalies (bar; mm/d; left *y*-axis) and SPI (red line; right *y*-axis). *y*-axis is reversed to highlight the severity of the 2019 Australian drought.

been comprehensively studied (Allan, 1988; McBride et al., 1983; Nicholls et al., 1996; Taschetto et al., 2009, 2010). El Niño events are usually accompanied by decreased precipitation over northeastern Australia via an increase in surface pressure associated with the Southern Oscillation (SO) western pole (Cai et al., 2011; Frauen et al., 2014), or by moving convection away from Australia as it prefers staying over the region of warm SSTs (Cai et al., 2010; Chung & Power, 2017). However, the Australian precipitation response to El Niño exhibits a certain degree of uncertainty partly owing to inter-El Niño variations in the tropical Pacific SST anomaly pattern (Lim et al., 2009; G. Wang & Hendon, 2007) and local SST conditions off the northern Australia coast (van Rensch et al., 2015). The inter-El Niño variations are mainly associated with occurrences of either so-called eastern-Pacific (EP) or central-Pacific (CP) El Niño events, characterized by maximum SST anomalies being located over the EP and CP, respectively (Ashok et al., 2007; Kao & Yu, 2009; Kug et al., 2009; Yeh et al., 2009). CP El Niño events tend to coincide with precipitation deficiencies over Australia, while EP El Niño events appear to be accompanied by less response in the region (G. Wang & Hendon, 2007), possibly due to the disturbance from other co-occurred SST anomalies. Local coastal SST anomalies have been proposed to be associated with atmospheric internal variability independent of El Niño (Brown et al., 2009), which may complicate isolating the El Niño signal in Australian precipitation anomalies (van Rensch et al., 2015).

A dipole SST anomaly structure between the western tropical Indian Ocean and the Sumatra-Java coast, referred to as the Indian Ocean Dipole (IOD) (Saji et al., 1999; Webster et al., 1999), is another prominent interannual climate variability pattern that exerts great impacts on Australian precipitation (Drosdowsky, 1993; Meyers, 1996; Nicholls, 1989; Vector &Franks, 2005). Concurrent with a CP El Niño event, a strong positive IOD event occurred in 2019 with comparable intensity to the strongest events that occurred in 1994 and 1997 (Doi et al., 2020; G. Wang et al., 2020). The exact nature of the ENSO-IOD relationship remains controversial, however, a line of research suggests that the IOD might be described as a natural mode

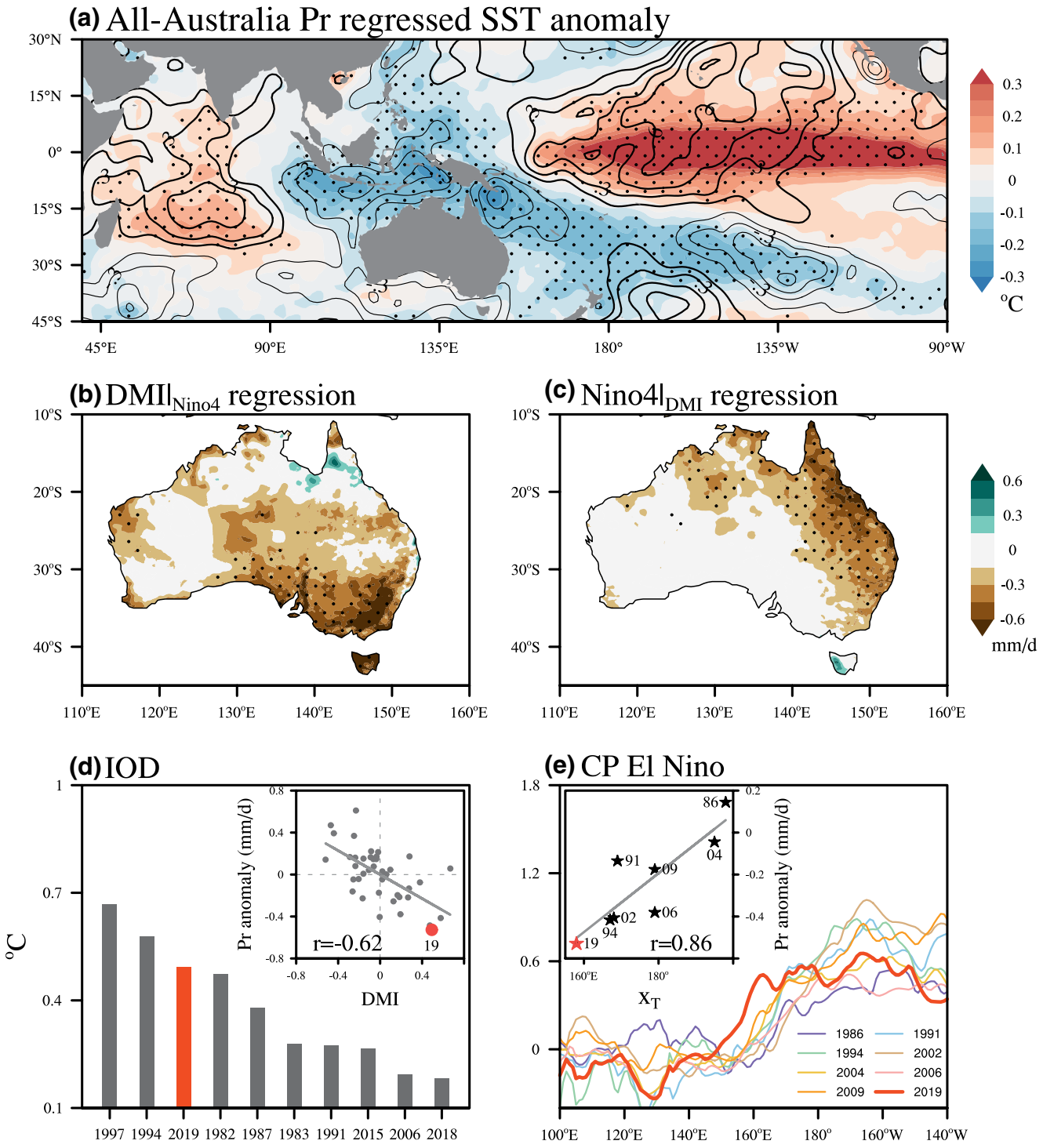

Figure 2. (a) Regressed SST anomalies (shading; °C) upon the all-Australian precipitation anomalies for May to December average, superimposed by the SST anomalies during May to December 2019 (contours; value interval: 0.15°C; black and gray for positive and negative values, respectively). The regression pattern was multiplied by −1 to focus on the SST anomalies associated with Australian precipitation deficiencies. Regressed May to December precipitation anomalies (mm/d) onto the (b) partial DMI and (c) partial Niño4 indices. Dots indicate regression coefficients that are statistically significant at the 95% confidence level. (d) May to December averaged DMI(°C) for the top 10 strongest Indian Ocean Dipole (DIO) events. The inset shows the scatterplot between the DMI and all-Australian precipitation anomalies ($r = -0.57$, significant at the 95% confidence level). (e) May to December averaged SST anomaly (°C) distribution along the equator (2°S-2°N) for CP El Niño events. The inset displays the scatterplot between the zonal location of CP El Niño and all-Australian precipitation anomalies ($r = 0.89$, significant at the 95% confidence level).

(Saji et al., 1999; Webster et al., 1999), which can also be triggered by remote forcings, particularly by ENSO variability (Li et al., 2003; Scott et al., 2009; Stuecker et al., 2017). The IOD typically excites atmospheric wave trains from the tropical Indian Ocean to extratropical Australia via an equivalent barotropic Rossby wave response (Ashok et al., 2003; Cai et al., 2011), which has been suggested as an important mechanism influencing precipitation over southern Australia (Cai et al., 2011; McIntosh & Hendon, 2018). The presence of a positive IOD event in conjunction with El Niño conditions can extend the precipitation deficiencies of either phenomena (Cai et al., 2011). So far, the underlying mechanisms driving the 2019 Australian extreme drought remain unclear. In this study, we use observations, reanalysis products, and numerical model experiments to investigate which role tropical thermal forcings played for the extreme precipitation deficiencies over Australia in 2019.

2. Data and Methodology

The SST data sets used in this study is based on the global sea ice and SST analyses from the Hadley Centre (HadISST) provided by the Met Office Hadley Centre (Rayner et al., 2003). The utilized precipitation data set is provided by the Australian Bureau of Meteorology (Jones et al., 2009). The atmospheric circulation data, including SLP and geopotential height, are derived from the National Centers for the Environmental Prediction-National Center for the Atmospheric Research (NCEP-NCAR) reanalysis (Kalnay et al., 1996). The horizontal resolution is 1° × 1° for the SST data set, 0.05° × 0.05° for the precipitation data set, and 2.5° × 2.5° for the circulation data set. The analyses cover the period from 1979 to 2019, and anomalies for all variables are computed by removing the monthly mean climatology (1979–2019). Our analysis is constrained to the satellite era after the late 1970s, considering that the SST pattern reconstruction before 1979 exhibits larger uncertainties (Smith et al., 1996), causing difficulties in accurately determining the zonal location of earlier El Niño events. Linear trends are removed from all data sets to avoid possible influences associated with global warming. The qualitative conclusions remain the same even if we use the raw data. All statistical significance tests are performed using the two-tailed Student's *t*-test.

El Niño events are identified according to the CPC's definition based on a threshold of 0.5°C of the Niño3.4 index (averaged SST anomaly in the domain of 5°S-5°N, 120°W-170°W) for five consecutive months. We calculate EP and CP indices (EPI and CPI) by using a mathematic rotation of the Niño3 (averaged SST anomaly in the domain of 5°S to 5°N, 90° to 150°W) and Niño4 (averaged SST anomaly in the domain of 5°S to 5°N, 160°E to 150°W) indices (Ren & Jin, 2011). The El Niño events with CPI greater than EPI are defined as CP El Niño events. We identify eight CP El Niño events (1986, 1991, 1994, 2002, 2004, 2006, 2009, and 2019). We further define a CP El Niño's zonal location and analyze its relationship with Australian precipitation anomalies. The zonal location of CP El Niño events is measured by the longitude of the maximum zonal gradient of the equatorial (2°S-2°N) averaged SST anomalies, which well captures the location of anomalous rising motion in the atmosphere west of the warm SST anomaly center (Zhang et al., 2015). The intensity of IOD events is measured by the Dipole Mode index (DMI) (Saji et al., 1999), which is defined as the SST anomaly difference between the western (10°S-10°N, 50°E-70°E) and eastern Indian Ocean (10°S-0°S, 90°E-110°E). The Standardized Precipitation Index (SPI) is one of the commonly used indices for meteorological drought from the perspective of accumulation, describing precipitation deficits on different time scales (McKee et al., 1993). Here a 6-month time scale is selected to focus on the seasonal to interannual drought over Australia. Drought classification according to the SPI value is based on the definition by the National Drought Mitigation Center (http://drought.unl.edu). Moderate drought denotes events with SPI values ranging from −1.5 to −1, while severe drought has values from −2 to −1.5, and the extreme drought values less than −2. Here, the SPI is chosen to focus on the drought condition associated with precipitation deficits while not taking into account temperature effects. Partial regression is employed to isolate impacts from ENSO and IOD individually. We refer to the regression with Niño4 when linearly removing the IOD associated impact by $\text{Niño4}|_{\text{DMI}}$. Similarly, the regression with the DMI is referred to by $\text{DMI}|_{\text{Niño4}}$ when excluding the linear impact of Niño4. Here, the Niño4 index is used to represent SST variability associated with CP El Niño. Similar results can be obtained by using the Niño3.4 index (albeit with weaker magnitude).

Numerical experiments are conducted using the Geophysical Fluid Dynamics Laboratory (GFDL) global Atmospheric Model version 2.1 (AM2.1) (Anderson et al., 2004), with a horizontal resolution of 2.5° longitude × 2° latitude and 24 vertical levels. Several sets of sensitive experiments are designed by forcing the

model with time-evolving CP SST anomaly forcing in the Pacific region (25°S-25°N, 150°E-90°W, the blue box in Figure S1) and IOD SST anomaly forcing in the tropical Indian Ocean region (25°S-25°N, 40°E-120°E, the black box in Figure S1) from April to December. The time-evolving SST anomalies are obtained by lead/lag regressing the SST anomalies from May to December onto the winter (Dec-Jan-Feb) Niño4 index and autumn (Sep-Oct-Nov) DMI index, respectively. Similar time-evolving SST anomalies can be derived by composite analyses and qualitative results remain the same. To inspect the individual role of CP El Niño and IOD events on Australian precipitation, we first force the model with observed Niño4 regressed (EXP_CP) and DMI regressed (EXP_IOD) SST anomalies, respectively. Both of the forcings are simultaneously prescribed to explore the combined effects of CP El Niño and IOD events (EXP_CP + IOD). We design other two sets of experiments to test the sensitivity of Australian precipitation responses to the zonal location of CP El Niño by shifting the prescribed CP warming eastward (EXP_CPEast) and westward (EXP_CPWest) by 10 degrees of longitude, respectively. Similarly, we also conduct two sets of experiments with regard to the intensity of IOD, multiplying the IOD regressed amplitude by a factor of 0.5 (EXP_IOD0.5), and 2 (EXP_IOD2). SST anomalies outside the forcing area are set to zero and only the positive loading in the Pacific region is used for the CP forcing. These SST anomaly patterns are then added to the 1979–2019 climatological SSTs. Each run is integrated for 20 years and the output from the last 15 years of the integration is used for our analysis. Anomalies in GFDL-AM2.1 are relative to a 20-year control simulation (EXP_CTRL) in which the model is forced only with seasonally varying climatological SSTs.

3. Results

We first investigate the time evolution of precipitation deficiencies over Australia during 2019 to display its extreme character (Figure 1). During March to April, Australia had precipitation deficits over its northwestern part. In the following months, the precipitation deficits extended to almost the entire Australian continent and persisted through the end of the year. The precipitation deficit pattern exhibited a clear seasonality with the center first being over the western and eastern coasts during May, shifting to the southeastern coast during June to October, and finally being located over northeastern Australia during November to December. Precipitation deficiencies increased following the seasonal evolution with all-Australian precipitation deficits ranging from about 20% to 40% during April to August, exceeding 50% in September to October, and reaching about 70% in November to December. We also use a 6-month SPI to measure the drought condition. According to this method, severe drought began to strike western Australia from May to August and then swept almost all of Australia from September to December. Especially, by the end of the year, most of the Australian continent was under extreme drought conditions. We hereinafter focus on the May to December average to investigate this long-lasting Australian drought event. The year 2019 was the driest year in decades in terms of the drought intensity (Figure 1b), as well as in terms of extent and duration (Figure S2). The extensive drought started to struck most of Australia since early spring, which is the most long-lasting large-scale drought since 1979 (Figure S2). The May to December cumulative precipitation was only about 110 mm, less than half the climatological value (Figure S3).

Concurrent with this long-lasting extensive drought, pronounced SST anomalies occurred in the Indo-Pacific oceans featuring a moderate CP El Niño and strong IOD-related SST anomaly pattern. This pattern is captured by a regression of SST anomalies with all-Australian precipitation anomalies (Figure 2a). The CP SST warming began in early 2019 and persisted into the winter season with an amplitude comparable to other CP El Niño events (Figure S4). CP El Niño events typically affect precipitation mainly over the near-tropical portion of Australia (Figure 2c) since the associated deep baroclinic component of the SO is trapped to the equatorial region (Figure S5a). Simultaneously, a positive IOD event developed during boreal summer and peaked during autumn, in an analogous manner to a typical IOD event but having above average intensity (Figure S4). Statistical diagnostics show that IOD events favor precipitation deficits over southern Australia (Figure 2b), which is tightly linked to IOD-associated equivalent barotropic Rossby wave trains (Chan et al., 2008) emanating from the tropical Indian Ocean toward southern Australia (Figures S5c and S5d).

We hypothesize that the combined effects of these two tropical thermal forcings in 2019 are essential to understand the mechanism that led to the extreme character of this Australian drought. Interestingly, we find that all-Australian precipitation anomalies have a stronger linear relationship ($r = 0.89$, statistically significant at the 95% confidence level) with the zonal location of a CP El Niño event (Figure 2e), than with

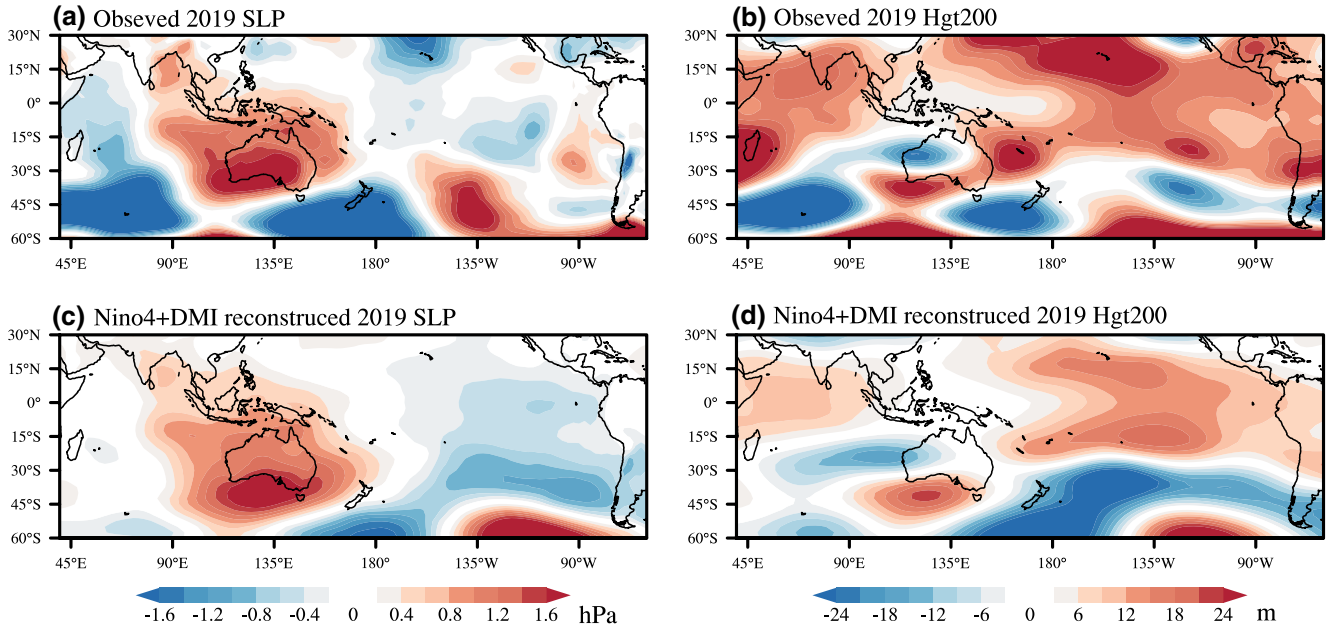

Figure 3. (a) Observed sea level pressure anomalies and (b) 200-hPa geopotential height anomalies (m) for May to December 2019. (c) Reconstruction of SLP anomalies and (d) 200-hPa geopotential height anomalies (m) based on the multiple linear regression using Niño4 and DMI.

its intensity as measured for instance by the Niño4 index ($r = -0.43$, insignificant even at the 80% confidence level). Australian precipitation deficiencies tend to increase as a CP El Niño event shifts its center farther westward. Besides, a negative correlation ($r = -0.57$, statistically significant at the 95% confidence level) is obtained between IOD intensity as measured by the DMI and Australian precipitation anomalies (Figure 2d), suggesting that Australian precipitation deficiencies increase as IOD intensity increases. During 2019 the westernmost-located CP El Niño event occurred concurrently with an extreme (third-ranking in amplitude) IOD event (Figures 2d and 2e), thus we expect that their combined effects could explain the extreme drought.

We reconstruct the atmospheric anomalies in 2019 by a linear regression to identify the relative importance of the two tropical SST forcings. Note that the nonorthogonality between the CP El Niño and the IOD events may prohibit simple superposition of their individual climate effects. The intensity of IOD events can be easily measured as the DMI in a linear regression equation, while the CP El Niño's zonal location cannot be effectively expressed due to its event dependence. Still, if we use both the Niño4 index and DMI as predictors in a linear reconstruction, the key atmospheric circulation anomalies associated with the 2019 Australian drought can be largely reproduced, including a sea level pressure (SLP) increase over Australia and its adjacent seas (Figures 3a and 3c) and atmospheric Rossby wave trains associated with the CP warming and IOD events (Figures 3b and 3d). However, the reconstructed upper-level pattern over the South Pacific, the so-called Pacific-Southern American (PSA) teleconnection (Ghil & Mo, 1991; Lau et al., 1994) emanating from the central tropical Pacific and arching toward South America (Figure S5b), is confined to the central and eastern Pacific (Figure 3d). It fails to capture the PSA-like pattern in 2019, which extended much further westward. Distinct from the traditional recognition that the PSA pattern is usually arching far away from the Australian continent (Cai et al., 2011), the westward-shifted PSA pattern in 2019 allowed impacts on the Australian climate by reducing precipitation locally. The importance CP El Niño zonal location is supported by the statistical analysis above (Figure 2e) and further by the correlation between CP El Niño zonal location and upper-level atmospheric circulation (Figure S6). However, the observational sample size is limited and CP El Niño events usually co-occur with other climate phenomena, such as the IOD. Therefore, we next explore the effect CP El Niño zonal location with a series of numerical model experiments.

The SST anomaly patterns used to force the various experiments are shown in Figure S1. We here show only upper-level atmospheric responses to highlight their sensitivity to different SST forcings since the low-level responses such as SLP exhibit a similar pattern with inter-experiment differences in intensity. In response

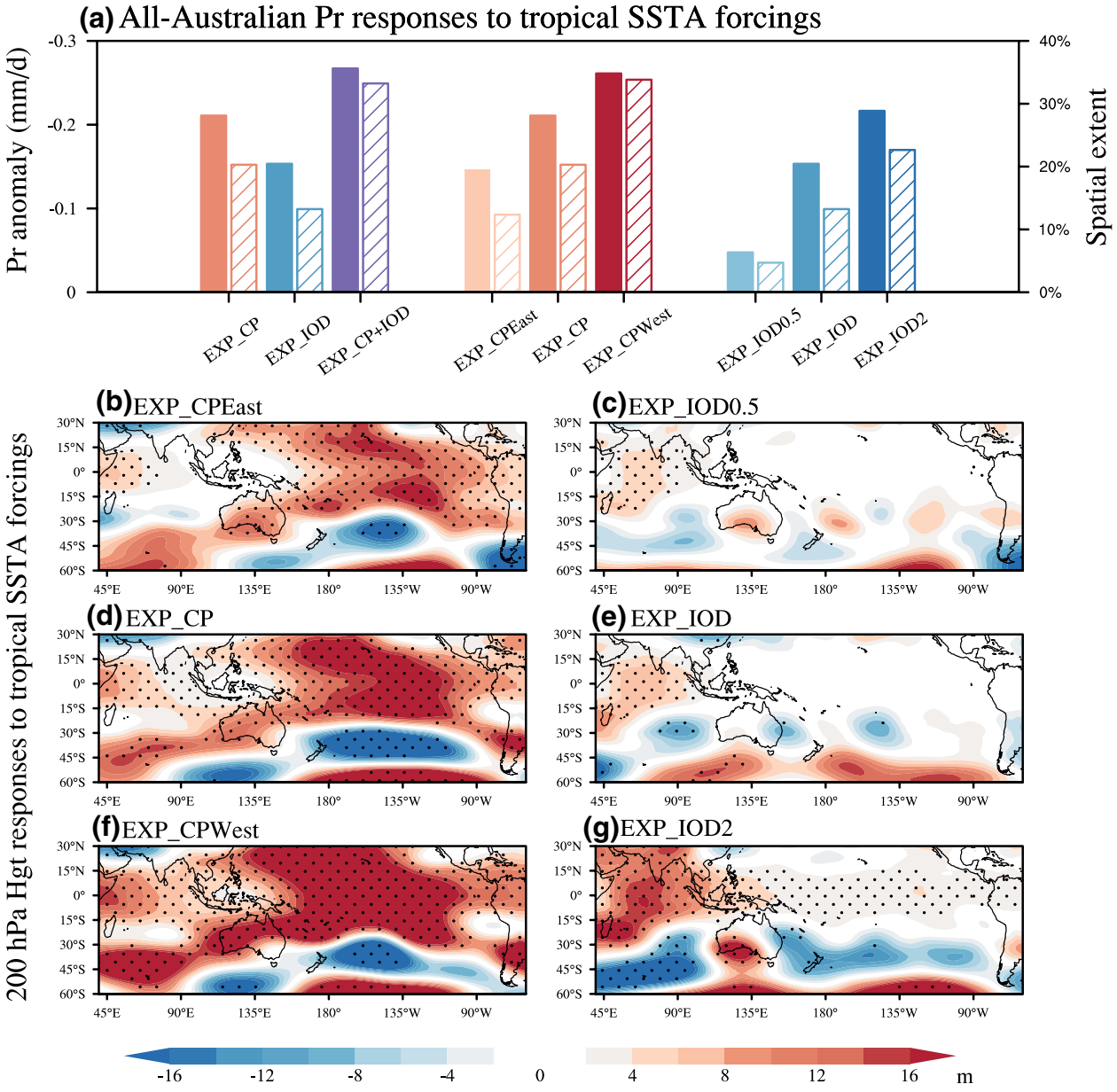

Figure 4. (a) Simulated all-Australian precipitation deficits (solid bar; mm/d; left *y*-axis) and corresponding spatial extents (striped bar; right *y*-axis) in experiments with different SST forcings (see details in Section 2). The spatial extent is defined as the percent of the grid points that have significant precipitation anomalies less than −0.2 mm/d. (b–g) 200-hPa geopotential height anomalies (m) in experiments with different SST forcings. Dots indicate composite values that are statistically significant at the 95% confidence level.

to the CP El Niño SST forcing, upper-tropospheric anticyclonic anomalies straddle the positive CP diabatic heating source in the central-western equatorial Pacific (Figure 4d) consistent with a deep baroclinic response (Gill, 1980; Matsuno, 1966). Simultaneously, upper-level divergence excites equivalent barotropic atmospheric Rossby wave trains toward off-equatorial South Pacific and America. The dominant characteristics of the observed atmospheric responses are well reproduced by the experiments. The atmospheric anomaly pattern over the Indian Ocean is different from the observed regressed Niño4 regression pattern, possibly due to absence of realistic Indian Ocean SST forcing. The experiment with IOD SST forcing can also well simulate the observed Rossby wave train curving southeastward from the tropical Indian Ocean toward the mid-latitudes (Figure 4e). Both experiments with the CP El Niño- and IOD SST forcings cause precipitation deficits over Australia despite some systematic biases, such as too weak responses over northern

Australia (Figure S7). When both SST forcing patterns are prescribed simultaneously, the simulated atmospheric anomaly pattern reproduces the observed pattern (Figure 3d) more realistically compared to the experiments with individual SST forcing patterns (Figure S8). Correspondingly, the Australian precipitation deficits are more severe and cover larger areas (Figures 4a and S7e), suggesting that the superimposed effects of the CP- and IOD-related SST anomalies tend to amplify their individual impacts on the Australian climate in terms of both the drought intensity and its spatial extent.

Next, we show two sets of experiments that are designed to depict the sensitivity of the Australian precipitation response to the zonal location of a CP El Niño event. When shifting the prescribed CP warming eastward by 10 degrees of longitude (EXP_CPEast), the upper-level Rossby wave response is displaced eastward with a relatively smaller amplitude (Figure 4b). In contrast, the atmospheric response is strengthened and extend westward (Figure 4f) when the CP SST forcing is shifted westward by 10 degrees of longitude (EXP_CPWest). These model experiments support our hypothesis that a farther westward-displaced CP warming (such as in 2019) exerts greater impacts on Australian climate via a modulation of the associated teleconnection patterns. Therefore, increased Australian precipitation deficits can be attributed to a more westward-displaced CP El Niño event (Figure 4a). Similarly, two sets of experiments are also conducted to investigate the sensitivity to IOD amplitude. In these experiments, the observed Rossby wave train pattern emanating from the tropical Indian Ocean can be approximately simulated, increasing in amplitude with increasing forcing (Figures 4c, 4e, and 4g). Accordingly, Australia receives more precipitation deficits with a strengthened IOD forcing (Figure 4a).

4. Discussion

In this study, we found that the long-lasting extreme Australian drought of 2019 can be attributed to the extraordinary combination of tropical Indo-Pacific thermal forcings, including the westernmost-located CP El Niño event and the third-most-extreme positive IOD event in the observational record (1979–2019). Both observations and numerical model experiments show that both farther westward-displaced CP El Niño events and stronger IOD events are conducive to Australian drought conditions. A similar combination of Indo-Pacific thermal conditions occurred in 1994 with the second ranking for both CP El Niño zonal location and IOD intensity (Figures 2d and 2e), which caused another devastating Australian drought (Figure 1b). We emphasize that Australian drought conditions can be severely impacted by tropical Indo-Pacific thermal conditions, which hints to potential predictability of future Australian extreme droughts analogous to the 2019 case several months in advance due to skill in seasonal tropical SST predictions (Doi et al., 2020). Our results further highlight the importance of pan-tropical SST patterns for regional climate impacts (e.g., Cai et al., 2019).

ENSO predictability has experienced a pronounced shift around 2000 with a skillful lead time decrease from about three seasons to one season (Hendon et al., 2009; McPhaden, 2012; W. Wang et al., 2010), which has been attributed to an ENSO regime shift with more frequent CP El Niño events occurring post-2000 (Zhang et al., 2019). The seasonal prediction of Australian precipitation is expected to struggle with the significantly reduced ENSO predictability in recent decades (Hendon et al., 2009; W. Wang et al., 2010). The current operational seasonal forecast skill for the IOD is limited to about one season lead time, which can be improved by utilizing the observed statistical ENSO-IOD relationship in combination with operational ENSO forecasts considering coupled Indo-Pacific climate variability (Doi et al., 2020; Luo et al., 2007; Zhao et al., 2019). Nevertheless, during recent decades the statistical El Niño-IOD relationship has weakened, likely due to an increased frequency of CP El Niño events (Zhang et al., 2015), suggesting their stronger independence (compared to EP El Niño events). Challenges for skillful seasonal prediction of extreme Australian droughts can be partially attributed to biases in current models in capturing both the zonal position of CP El Niño events as well as the intensity of IOD events realistically. A larger effort needs be made to improve model performances in accurately simulating Indo-Pacific SST anomalies as well as their remote climate impacts.

In a warming world, both CP El Niño and extreme positive IOD events are projected to become more frequent (Cai et al., 2014; Yeh et al., 2009). While these projections remain to be further refined as coupled general circulation models continue to evolve, these studies hint at an increased probability in co-occurrence

of these two phenomena with global warming. This could increase the risk of severe Australian droughts, causing extensive damage to vegetation ecosystems, drinking-water shortages, and substantial pecuniary loss. These tropical-induced extreme events are expected to be further intensified by the long-term aridification trends in Australia due to global warming (Trenberth et al., 2014). Other process in the climate system such as the stratospheric polar vortex (Lim et al., 2019) and temperature extremes (via its impact on evapotranspiration), likely also contributed to this devasting drought, which should be further explored in future studies.

Data Availability Statement

The data used to reproduce the results of this paper are located at https://www.metoffice.gov.uk/hadobs/hadisst/data/download.html, http://www.bom.gov.au/climate/maps/rainfall/ and https://www.esrl.noaa.gov/psd/data/gridded/data.ncep.reanalysis.html.

Acknowledgments
This work was supported by the National Nature Science Foundation of China (41675073) and the National Key Research and Development Program (2018YFC1506002). This is SOEST publication 11210 and IPRC contribution 1495.

References

Allan, R. J. (1988). El Niño-Southern Oscillation influences in the Australasian region. *Progress in Physical Geography*, *12*, 313–348. https://doi.org/10.1177/030913338801200301

Anderson, J. L., Balaji, V., Broccoli, A. J., Cooke, W. F., Delworth, T. L., Dixon, K. W., et al. (2004). The New GFDL Global Atmosphere and Land Model AM2-LM2: Evaluation with prescribed SST simulations. *Journal of Climate*, *17*, 4641–4673.

Ashok, K., Behera, S. K., Rao, S. A., Weng, H., & Yamagata, T. J. (2007). El Niño Modoki and its possible teleconnection. *Geophysical Research Letters*, *112*, C11007. https://doi.org/10.1029/2006JC003798

Ashok, K., Guan, Z., & Yamagata, T. (2003). Influence of the Indian Ocean Dipole on the Australian winter rainfall. *Geophysical Research Letters*, *30*, 1821. https://doi.org/10.1029/2003GL017926

Brown, J. N., McIntosh, P. C., Pook, M. J., & Risbey, J. S. (2009). An investigation of the links between ENSO flavors and rainfall processes in southeastern Australia. *Monthly Weather Review*, *137*, 3786–3795.

Bureau of Meteorology. (2019). *Drought conditions in Australia and impact on water resources in the Murray-Darling Basin*. Special Climate Statement, 70. Retrieved from http://www.bom.gov.au/climate/current/statements/scs70.pdf

Bureau of Meteorology. (2019). *Dangerous bushfire weather in Spring 2019*. Special Climate Statement, 70. Retrieved from http://www.bom.gov.au/climate/current/statements/scs72.pdf

Cai, W., Santoso, A., Wang, G., Weller, E., Wu, L., Ashok, K., et al. (2014). Increased frequency of extreme Indian Ocean Dipole events due to greenhouse warming. *Nature*, *510*, 254–258.

Cai, W., Wu, L., Lengaigne, M., Li, T., McGregor, S., Kug, J., et al. (2019). Pantropical climate interactions. *Science*, *363*, eaav4236.

Cai, W., van Rensch, P., Cowan, T., & Hendon, H. H. (2011). Teleconnection pathways of ENSO and the IOD and the mechanisms for impacts on Australian rainfall. *Journal of Climate*, *24*, 3910–3923.

Cai, W., van Rensch, P., Cowan, T., & Sullivan, A. (2010). Asymmetry in ENSO teleconnection with regional rainfall, its multidecadal variability, and impact. *Journal of Climate*, *23*, 4944–4955.

Chan, S. C., Behera, S. K., & Yamagata, T. (2008). Indian Ocean dipole influence on South American rainfall. *Geophysical Research Letters*, *35*, L14S12. https://doi.org/10.1029/2008GL034204

Chung, C., & Power, S. (2017). The non-linear impact of El Niño, La Niña and the Southern Oscillation on seasonal and regional Australian precipitation. *Journal of Southern Hemisphere Earth System Science*, *67*, 25–45.

Doi, T., Behera, S. K., & Yamagata, T. (2020). Predictability of the super IOD event in 2019 and its link with El Niño Modoki. *Geophysical Research Letters*, *47*(7), e2019GL086713. https://doi.org/10.1029/2019GL086713

Drosdowsky, W. (1993). Potential predictability of winter rainfall over southern and eastern Australia using Indian Ocean sea-surface temperature anomalies. *Australian Meteorological Magazine*, *42*, 1–6.

Ell, K. (2020). *Moody's analytics research, Weekly market outlook*. Retrieved from https://www.moodysanalytics.com/-/media/article/2020/weekly-market-outlookovervalued-equities-increase-corporate-credits-downside-risk.pdf

Frauen, C., Dommenget, D., Tyrrell, N., Rezny, M., & Wales, S. (2014). Analysis of the nonlinearity of El Niño-Southern Oscillation teleconnections. *Journal of Climate*, *27*, 6225–6244.

Gallant, A. J. E., Hennessy, K. J., & Risbey, J. (2007). Trends in rainfall indices for six Australian regions: 1910–2005. *Australian Meteorological Magazine*, *56*, 223–241.

Ghil, M., & Mo, K. C. (1991). Intraseasonal oscillations in the global atmosphere. Part II: Southern Hemisphere. *Journal of the Atmospheric Sciences*, *48*, 780–790.

Gill, A. E. (1980). Some simple solutions for heat-induced tropical circulation. *Quarterly Journal of the Royal Meteorological Society*, *106*, 447–462. https://doi.org/10.1002/qj.49710644905

Hendon, H. H., Lim, E., Wang, G., Alves, O., & Hudson, D. (2009). Prospects for predicting two flavors of El Niño. *Geophysical Research Letters*, *36*, L19713. https://doi.org/10.1029/2009GL040100

Jones, D. A., Wang, W., & Fawcett, R. (2009). High-quality spatial climate data-sets for Australia. *Australian Meteorological and Oceanographic Journal*, *58*, 233–248.

Kalnay, E., Kanamitsu, M., Kistler, R., Collins, W., Deaven, D., Gandin, L., et al. (1996). The NCEP/NCAR 40-Year reanalysis project. *Bulletin of the American Meteorological Society*, *77*, 437–447.

Kao, H.-Y., & Yu, J.-Y. (2009). Contrasting Eastern-Pacific and Central-Pacific types of ENSO. *Journal of Climate*, *22*, 615–632.

King, A. D., Pitman, A. J., Henley, B. J., Ukkola, A. M., & Brown, J. R. (2020). The role of climate variability in Australian drought. *Nature Climate Change*, *10*, 177–179.

Kug, J.-S., Jin, F.-F., & An, S.-I. (2009). Two types of El Niño events: Cold tongue El Niño and warm pool El Niño. *Journal of Climate*, *22*, 1499–1515.

Lau, M. K., Sheu, P. J., & Kang, I. S. (1994). Multiscale low-frequency circulation modes in the global atmosphere. *Journal of the Atmospheric Sciences*, *51*, 2753–2750.
Li, T., Wang, B., Chang, C.-P., & Zhang, Y. (2003). A theory for the Indian Ocean Dipole-Zonal Mode. *Journal of the Atmospheric Sciences*, *60*, 2119–2135.
Lim, E.-P., Hendon, H. H., Boschat, G., Hudson, D., Thompson, D. W., Dowdy, A. J., & Arblaster, J. M. (2019). Australian hot and dry extremes induced by weakenings of the stratospheric polar vortex. *Nature Geoscience*, *12*, 896–901.
Lim, E.-P., Hendon, H. H., Hudson, S., Wang, G., & Alves, O. (2009). Dynamical forecast of inter-El Niño variations of tropical SST and Australia spring rainfall. *Monthly Weather Review*, *137*, 3796–3810.
Luo, J.-J., Masson, S., Behera, S., & Yamagata, T. (2007). Experimental forecasts of the Indian Ocean dipole using a coupled OAGCM. *Journal of climate*, *20*(10), 2178–2190.
Matsuno, T. (1966). Quasi-geostrophic motions in the equatorial area. *Journal of the Meteorological Society of Japan*, *44*(1), 25–43.
McBride, J. L., & Nicholls, N. (1983). Seasonal relationships between Australian rainfall and the Southern Oscillation. *Monthly Weather Review*, *111*, 1998–2004. https://doi.org/10.1175/1520-0493
McIntosh, P. C., & Hendon, H. H. (2018). Understanding Rossby wave trains forced by the Indian Ocean Dipole. *Climate Dynamics*, *50*, 2783–2798.
McKee, T. B., Doeskin, N. J., & Kleist, J. (1993). The relationship of drought frequency and duration to time scales. *Proceedings of the 8th Conference on Applied Climatology* (Vol. *17*, pp. 179–184). Boston, MA: American Meteorological Society.
McPhaden, M. J. (2012). A 21st century shift in the relationship between ENSO SST and warm water volume anomalies. *Geophysical Research Letters*, *39*, L09706. https://doi.org/10.1029/2012GL051826
McPhaden, M. J., Zebiak, S. E., & Glantz, M. H. (2006). ENSO as an integrating concept in Earth science. *Science*, *314*, 1740–1745.
Meyers, G. (1996). Variation of the Indonesian throughflow and the El Niño-Southern Oscillation. *Journal of Geophysical Research*, *101*, 12255–12263.
Nicholls, N. (1989). Sea surface temperatures and Australian winter rainfall. *Journal of Climate*, *2*(9), 965–973.
Nicholls, N., Lavery, B., Frederiksen, C., Drosdowsky, W., & Torok, S. (1996). Recent apparent changes in relationships between the El Niño-Southern Oscillation and Australian rainfall and temperature. *Geophysical Research Letters*, *23*, 3357–3360. https://doi.org/10.1029/96GL03166
Philander, S. G. (1990). *El Niño, La Niña, and the Southern Oscillation*. San Diego, CA: Academic.
Rayner, N. A., Parker, D. E., Horton, E. B., Folland, C. K., Alexander, L. V., & Rowell, D. P. (2003). Global analyses of sea surface temperature, sea ice, and night marine air temperature since the late nineteenth century. *Journal of Geophysical Research*, *108*, 4407. https://doi.org/10.1029/2002JD002670
Ren, H.-L., & Jin, F.-F. (2011). Niño indices for two types of ENSO. *Geophysical Research Letters*, *38*, L04704. https://doi.org/10.1029/2010GL046031
Saji, N. H., Goswami, B. N., Vinayachandran, P. N., & Yamagata, T. (1999). A dipole in the tropical Indian Ocean. *Nature*, *401*, 360–363.
Scott, A. F., Xiang, S.-P., & McCreary, J. P., Jr. (2009). Indian Ocean circulation and climate variability. *Reviews of Geophysics*, *47*, RG1002. https://doi.org/10.1029/2007RG000245
Smith, T. M., Reynolds, R. W., Livezey, R. E., & Stokes, D. C. (1996). Reconstruction of historical sea surface temperatures using empirical orthogonal functions. *Journal of Climate*, *9*(6), 1403–1420.
Stuecker, M. F., Timmermann, A., Jin, F.-F., Chikamoto, Y., Zhang, W., Wittenberg, A. T., et al. (2017). Revisiting ENSO/Indian Ocean Dipole phase relationships. *Geophysical Research Letters*, *44*(5), 2481–2492. https://doi.org/10.1002/2016GL072308
Taschetto, A. S., & England, M. H. (2009). El Niño Modoki impacts on Australian rainfall. *Journal of Climate*, *22*, 3167–3174.
Taschetto, A. S., Haarsma, R. J., Gupta, A. S, Ummenhofer, C. C., Hill, K. J., & England, M. H. (2010). Australian Monsoon Variability Driven by a Gill–Matsuno-Type Response to Central West Pacific Warming. *Journal of Climate*, *23*(18), 4717–4736. https://doi.org/10.1175/2010jcli3474.1
Trenberth, K. E., Dai, A., van der Schrier, G., Jones, P. D., Barichivich, J., Briffa, K. R., & Sheffield, J. (2014). Global warming and changes in drought. *Nature Climate Change*, *4*(1), 17–22. https://doi.org/10.1038/nclimate2067
Ummenhofer, C. C., England, M. H., McIntosh, P. C., Meyers, G. A., Pook, M. J., Risbey, J. S., et al. (2009). What causes southeast Australia's worst droughts? *Geophysical Research Letters*, *36*(4), L04706. https://doi.org/10.1029/2008gl036801
van Rensch, P., Gallant, A. J. E., Cai, W., & Nicholls, N. (2015). Evidence of local sea surface temperatures overriding the southeast Australian rainfall response to the 1997–1998 El Niño. *Geophysical Research Letters*, *42*, 9449–9456. https://doi.org/10.1002/2015GL066319
Verdon, D. C., & Franks, S. W. (2005). Indian Ocean sea surface temperature variability and winter rainfall: Eastern Australia. *Water Resources Research*, *41*, W09413. https://doi.org/10.1029/2004WR003845
Wang, G., Cai, W., Yang, K., Santoso, A., & Yamagata, T. (2020). A unique feature of the 2019 extreme positive Indian Ocean Dipole event. *Geophysical Research Letters*, *47*, e2020GL088615. https://doi.org/10.1029/2020GL088615
Wang, W., Chen, M., & Kumar, A. (2010). An assessment of the CFS real time seasonal forecasts. *Weather and Forecasting*, *25*, 950–969.
Wang, G., & Hendon, H. H. (2007). Sensitivity of Australian rainfall to Inter–El Niño variations. *Journal of Climate*, *20*, 4211–4226.
Webster, P. J., Moore, A. M., Loschnigg, J. P., & Leben, R. R. (1999). Coupled oceanic-atmospheric dynamics in the Indian Ocean during 1997–98. *Nature*, *401*, 356–360.
Yeh, S.-W., Kug, J.-S., Dewitte, B., Kwon, M.-H., Kirtman, B. P., & Jin, F.-F. (2009). El Niño in a changing climate. *Nature*, *461*(7263), 511–514. https://doi.org/10.1038/nature08316
Zhang, W., Li, S., Jin, F.-F., Xie, R., Liu, C., Stuecker, M. F., & Xue, A. (2019). ENSO regime changes responsible for decadal phase relationship variations between ENSO sea surface temperature and warm water volume. *Geophysical Research Letters*, *46*(13), 7546–7553. https://doi.org/10.1029/2019gl082943
Zhang, W., Wang, Y., Jin, F.-F., Stuecker, M. F., & Turner, A. G. (2015). Impact of different El Niño types on the El Niño/IOD relationship. *Geophysical Research Letters*, *42*, 8570–8576. https://doi.org/10.1002/2015GL065703
Zhao, S., Jin, F.-F., & Stuecker, M. F. (2019). Improved predictability of the Indian Ocean Dipole using seasonally modulated ENSO forcing forecasts. *Geophysical Research Letters*, *46*, 9980–9990. https://doi.org/10.1029/2019GL084196